Materials Today Communications 40 (2024) 109591

Contents lists available at ScienceDirect

Materials Today Communications

journal homepage: www.elsevier.com/locate/mtcomm

Exploring the thermal and mechanical properties of PAI-Graphene monolayers and nanotubes: Insights from molecular dynamics simulations

Rodrigo A.F. Alves [a,b], William F. Giozza [c], Luiz A. Ribeiro Jr [a,b], Marcelo L. Pereira Jr [c,*]

[a] University of Brasília, Institute of Physics, 70910-900, Brasília, Brazil
[b] Computational Materials Laboratory, LCCMat, Institute of Physics, University of Brasília, 70910-900, Brasília, Brazil
[c] University of Brasília, College of Technology, Department of Electrical Engineering, 70910-900, Brasília, Brazil

ARTICLE INFO

Keywords:
2D carbon allotropes
PAI-Graphene
Monolayer
Nanotube
Mechanical properties
Thermal properties

ABSTRACT

Two-dimensional (2D) materials are widely applicable in emerging technologies, with graphene remaining a focal point of interest. Among the computationally designed 2D carbon allotropes is PAI-Graphene (PAI-G), formed through the lateral polymerization of molecules containing 5- and 6-membered rings, specifically Polimerized as-Indacene. This study employs reactive molecular dynamics simulations to explore the thermal and mechanical properties of PAI-G monolayers and nanotubes using the AIREBO-M potential. The results reveal that the melting point of PAI-G is 3200 K, significantly lower than that of graphene. Anisotropic behavior in elastic properties is observed in PAI-G monolayers, with similar trends seen in nanotubes of varying chiralities. The Young's modulus values for these systems range between 650 and 900 GPa. Furthermore, the analysis of nanotubes across different diameters unveils a correlation between diameter and elastic constants. A Machine Learning Interatomic Potential (MLIP) was trained to confirm the appropriateness of the standard parameterized AIREBO-M potential for describing the thermomechanical behavior of PAI-G.

1. Introduction

Over the past three decades, there has been extensive research on two-dimensional (2D) materials [1]. In 2004, graphene was successfully obtained in experiments [2]. This breakthrough marked a significant turning point, leading to a notable surge in research activity within the field of nanoscience [3]. Studies on graphene have highlighted its remarkable properties, including high mechanical strength, lightness, transparency, and outstanding electrical and thermal conductivity [4,5]. These attributes have sparked immense interest in graphene and positioned it as a promising material for a wide range of applications, such as electronic devices [6], energy storage systems [7], and sensor technologies [8]. Following the successful synthesis of graphene, considerable efforts have been directed toward the theoretical proposition and experimental synthesis of new materials with properties comparable to or even surpassing those of graphene. This concerted endeavor has led to the discovery and development of various carbon allotropes exhibiting similar characteristics [9–20].

The large-scale production of these 2D materials is increasingly imperative to make their applications globally accessible [1]. In this context, several 2D carbon allotropes, such as γ-graphene [21], monolayer amorphous carbon [22], biphenylene monolayer [19], and fullerene network [20], have been synthesized and extensively discussed in the literature. The versatile application potential of these materials across various domains underscores the indispensability of ongoing investigations in this field [23].

While synthesizing novel materials poses significant challenges, their theoretical proposals offer valuable insights and potential avenues for experimental exploration [24,25]. The theoretical proposals constitute the primary focus for the computational modeling of novel structures [26,27]. Generally, the presentation of a novel computationally designed structure is intended to contribute to the ongoing discourse surrounding innovative 2D carbon-based material design [28,29], acknowledging its theoretical nature and potential impact if successfully synthesized. The importance of experimental validation for the computational proposed materials is fully understood, and the recognition of the complexity and time-consuming nature of the journey from theoretical proposal to laboratory synthesis is present. However, optimism about the feasibility of realizing this structure remains, especially considering the recent advancements in synthesizing biphenylene [19] and monolayer fullerene [20] networks.

Recently, a novel carbon allotrope was proposed featuring a unique arrangement of polymerized as-indacene molecules in a zigzag pattern (PAI-G) [11]. This material falls into the pure crystalline topological semimetals category, characterized by anisotropic Fermi velocities

* Corresponding author.
E-mail address: marcelo.lopes@unb.br (M.L. Pereira Jr).

https://doi.org/10.1016/j.mtcomm.2024.109591
Received 30 January 2024; Received in revised form 13 June 2024; Accepted 15 June 2024
Available online 21 June 2024

reaching values as high as 7×10^5 m/s. PAI-G garners attention for its intriguing electronic properties, boasting two ideally located Dirac cones at the Fermi level. PAI-G exhibits monoatomic thickness and a smooth, featureless surface. In terms of hybridization, PAI-G exclusively adopts the sp^2 configuration. Furthermore, it maintains its intrinsic metallicity even after Li/Na adsorption, ensuring favorable conductivities as an electrode [11]. PAI-G also demonstrates a significantly low open-circuit voltage (0.342–0.190 V for Li, 0.339–0.233 V for Na) and diffusion barriers of 0.34 eV for Li and 0.17 eV for Na, suggesting its potential application as an anode [11,30].

PAI-G presents a lattice structure composed of 5, 6, and 7 rings of carbon atoms, which was obtained using an evolutionary algorithm based on the USPEX code [31]. Another allotrope similar to PAI-G is PSI-Graphene (PSI-G, Polymerized S-Indacene), which shares the same types of rings but is arranged differently [32,33]. In addition to the electronic characteristics explored in PAI-G, a comprehensive understanding of its thermal and mechanical properties is needed. Such insights are crucial for the thorough characterization and potential synthesis of this material in the future.

This study conducted fully atomistic simulations using reactive molecular dynamics (MD) to investigate the thermal and mechanical properties of PAI-G. The stress–strain characteristics of monolayers and nanotubes (with different diameters and chiralities) were discussed. A heat-ramp protocol was also employed to study its thermal properties. Our results demonstrate that Young's modulus of PAI-G varies between approximately 650 and 900 GPa, with its critical temperature (melting) at approximately 3200 K, significantly lower than that of graphene. A Machine Learning Interatomic Potential (MLIP) was trained to confirm the appropriateness of the standard parameterized potential used for describing the thermomechanical behavior of PAI-G.

2. Methodology

To characterize the mechanical and thermal properties of PAI-G monolayers and nanotubes (PAI-GNTs), reactive MD simulations were conducted using the LAMMPS [34,35] software and the modified Adaptive Empirical Reactive Intermolecular Bond Order (AIREBO-M) [36] potential. Reactive potentials, known for their accuracy in predicting chemical bond breaking and formation, have been successfully employed in numerous prior studies to investigate the thermomechanical properties of 2D carbon-based materials, as presented in these Refs. [10,37–39].

While the standard AIREBO potential has been widely used for hydrocarbons to study dynamic bonding processes under ambient conditions [40], its reliance on a Lennard–Jones (LJ) potential for intermolecular interactions poses limitations. Specifically, the LJ potential's unphysically divergent power-law repulsion can cause AIREBO to falter when applied to systems under high pressure. To address this issue, the modified potential, AIREBO-M, replaces the singular LJ potential with a Morse potential [36]. This modification enhances intermolecular steric repulsions while preserving the ambient thermodynamics of the original potentials to the greatest extent possible. A Machine Learning Interatomic Potential (MLIP) was trained to confirm the appropriateness of the standard parameterized AIREBO-M potential used for describing the thermomechanical behavior of PAI-G. The supplementary material presents details on the MLIP simulations.

The thermal and mechanical characteristics of PAI-G were assessed in two different arrangements: monolayers and nanotubes. For nanotubes, variations in diameter and chirality were explored, with the longitudinal direction aligned parallel to the z axis. Periodic boundary conditions in the x and y directions for monolayers and in the z direction for nanotubes were applied. A vacuum distance of 250 Å was maintained in all systems to prevent interaction with images in the non-periodic directions.

Seven distinct types of structures based on PAI-G were analyzed. The 2D case, with an area of 1.54 μm^2 containing 5712 carbon atoms, was derived from a supercell with $14 \times 17 \times 1$ replications of the unit cell, based on the lattice vectors $\vec{a}$ and $\vec{b}$ (see Fig. 1). Regarding 1D systems, the structures were categorized into two distinct classes based on their chiralities. The chiral vector $\vec{C}_h = m \cdot \vec{a}_1 + n \cdot \vec{b} = (m, n)$ is defined by the number of replications in different directions of the unit cell, where m and n are integers.

Table 1
Structural PAI-GNTs information.

Chirality (m,n)	Length (Å)	Diameter (Å)	Number of atoms
(0,2)	98.95	4.59	528
(0,5)	98.95	11.47	1320
(0,9)	98.95	20.64	2376
(2,0)	100.88	5.73	672
(4,0)	100.88	11.45	1344
(7,0)	100.88	20.04	2352

The chiral vector determines the circumference length of the nanotubes and, consequently, the winding direction of the systems. In this way, the nanotubes are distinguished based on their chiral vector. PAI-GNT(m,n) is the nanotube whose winding occurs in the direction of the vector $\vec{C}_h = (m,n)$, and the diameter is $d_{m,n} = |\vec{C}_h|/\pi = (1/\pi)\sqrt{m^2 \cdot |\vec{a}|^2 + n^2 \cdot |\vec{b}|^2}$. The nanotube length is determined by the magnitude of the translational vector $\vec{T} = t_1 \cdot \vec{a} + t_2 \cdot \vec{b}$, which is perpendicular to $\vec{C}_h$, i.e., $\vec{C}_h \cdot \vec{T} = 0$, with t_1 and t_2 being integers.

Here, two chiralities and three distinct diameters were chosen. The obtained chiralities are $(m,0)$ and $(0,n)$. In this perspective, $d_{(m,0)} = m \cdot |\vec{a}|/\pi$ and $d_{(0,n)} = n \cdot |\vec{b}|/\pi$, with translational vectors $\vec{T}_{(m,0)} = t_2 \cdot \vec{b}$ and $\vec{T}_{(0,n)} = t_1 \cdot \vec{a}$, respectively. For a better comparison between chiralities, three similar diameters were chosen in each case, with dimensions approximately 5, 10, and 20 Å (see Fig. 2). For the length of the nanotubes, according to the presentation above, $t_1 = 11$ and $t_2 = 14$ were chosen to obtain systems with lengths close to 100 Å. Structural information for the nanotubes is presented in Table 1.

The equations of motion were solved using the Velocity-Verlet algorithm, with an integration time step of 0.1 fs [41]. In all simulations, the isobaric-isothermal ensemble with the Nosé–Hoover thermostat [42] was employed to maintain a constant temperature. Initially, a 50 ps equilibration process was undertaken to eliminate internal residual stress in the structure at 300 K. Following this equilibration process and ensuring zero pressure and thermalization at room temperature, two distinct protocols were executed for heating and strain. To comprehensively characterize the thermal and mechanical properties of PAI-G, each simulation was repeated five times with different sets of initial velocities. The physical characteristics of these systems were determined from the averages and errors of the samples.

To analyze how PAI-G responds to temperature changes, we subjected the system to a gradual temperature increase from 300 to 10000 K at approximately 4×10^{-3} K per time step. By calculating the system's total energy and monitoring its temperature, the melting temperature was determined. Additionally, snapshots of significant moments were captured to provide insights into the structural evolution of the system as temperature rose.

Uniaxial strains are assigned to each system for the tensile loading simulations of PAI-G. For 2D systems, strains were applied in the x and y directions, while for PAI-GNTs, strains were applied in the z direction. In the case of monolayers, the NPT ensemble was employed to allow the system to adjust in directions perpendicular to the strain, accounting for Poisson's effect. The strain was applied by deforming the simulation box at a rate of 10^{-6} fs^{-1} until reaching a maximum strain of 50% of the original structure size in the evaluated direction (a total of 5 million integration steps). Physical information about the system was extracted, including total stress, Young's modulus, and critical strain and stress. Like in the melting case, MD snapshots were also captured of specific strain moments for visualization using the VMD (Visual Molecular Dynamics [43]) software (Humphrey et al. 1996).

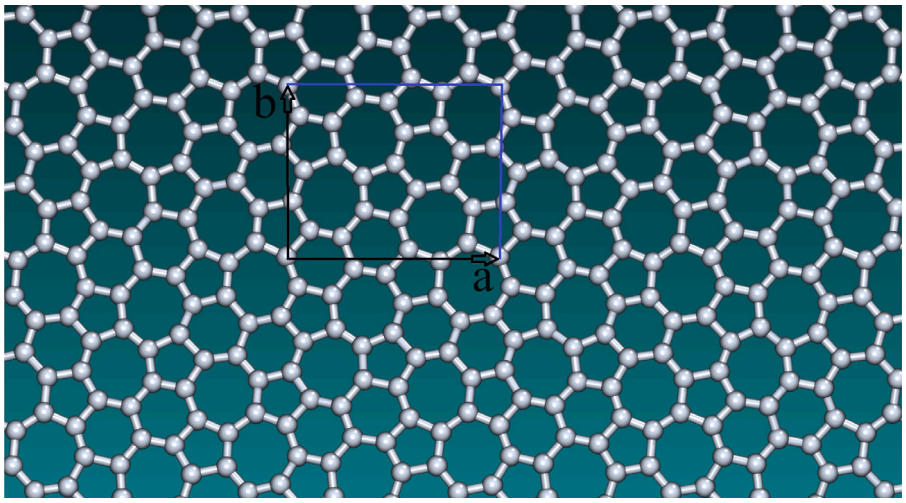

Fig. 1. Monolayer PAI-G, enlarged for better visualization of its unit cell, which has a rectangular shape and is composed of 24 atoms, defined by the lattice vectors $\vec{a}$ and $\vec{b}$. The dimensions of the unit cell are $|\vec{a}| = 8.995$ and $|\vec{b}| = 7.206$ Å.

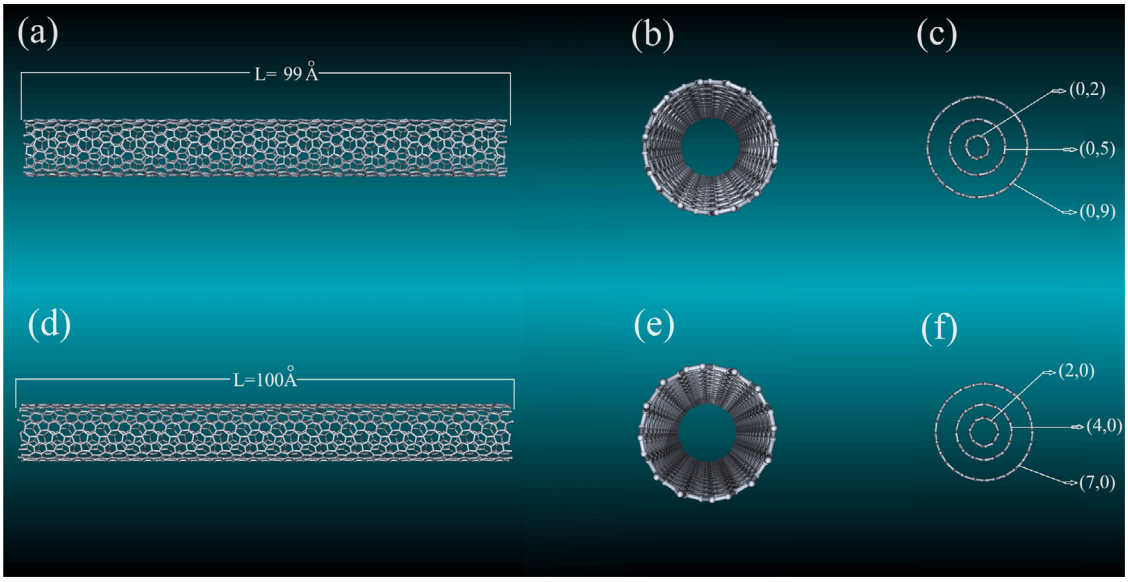

Fig. 2. Schematic representation of the nanotubes under evaluation, along with their respective dimensions. The upper section of the figure presents the lateral (a) and frontal (b) views of PAI-GNT(0,5) to examine the edge type of the systems $(0, n)$ alongside a comparison of the investigated diameters for this chirality (c). The lower section provides the lateral (d) and frontal (e) views of the PAI-GNT$(m, 0)$ systems alongside a comparison of the investigated diameters for this chirality (f). Additional structural details about the systems can be found in Table 1.

3. Results

3.1. Thermal characterization

To examine how PAI-G monolayers respond to changes in the thermal bath temperature, the total energy and system temperature were monitored at intervals of 100 fs over a simulation time of 250 ps. The thermal bath temperature ranged from 300 K to 10000 K. Fig. 3 depicts the correlation between the temperature over time with the total energy of the system and the thermal capacity. Green curves represent the total energy as a function of temperature for five sets of initial velocities. The total capacity, depicted by orange curves, is represented as a function of temperature for the same five sets of initial velocities. The system's total volume remains constant since the canonical ensemble (NVT) was employed. Therefore, the heat capacity, defined as $C_V = \delta Q/dT = (\partial U/\partial T)_V$, was evaluated and normalized.

Fig. 3 shows that the five initial configurations studied exhibit a convergence to the same behavior. The total energy increases with temperature, delineating four distinct regimes defined by temperature ranges: 300 to 2000 K, 2000 to 3000 K, 3000 to 6000 K, and above 6000 K. Up to 2000 K, PAI-G demonstrates a linear increase in total energy, indicating no phase change within the system. This trend illustrates the thermal stability of PAI-G up to this critical temperature, rendering it suitable for various applications subjected to high-temperature fluctuations. Between 2000 and 3000 K, the melting process of the system initiates, with the melting temperature defined as the point where the most significant variation in total system energy occurs (about 3200 K for all sets of initial velocities). This melting temperature is considerably lower than the one reported for graphene, approximately 4510 K [44]. In the 3000 to 6000 K range, the system exhibits the clustering of fragments that disintegrate as the temperature increases, leading to a sub-peak in the heat capacity within this region. Beyond 6000 K, the system displays gas-like characteristics, with the rise in energy in this new phase reverting to a linear trend.

In line with the variations in the total energy of PAI-G, as presented in Figs. 3, 4 shows snapshots of the heating process for the PAI-G

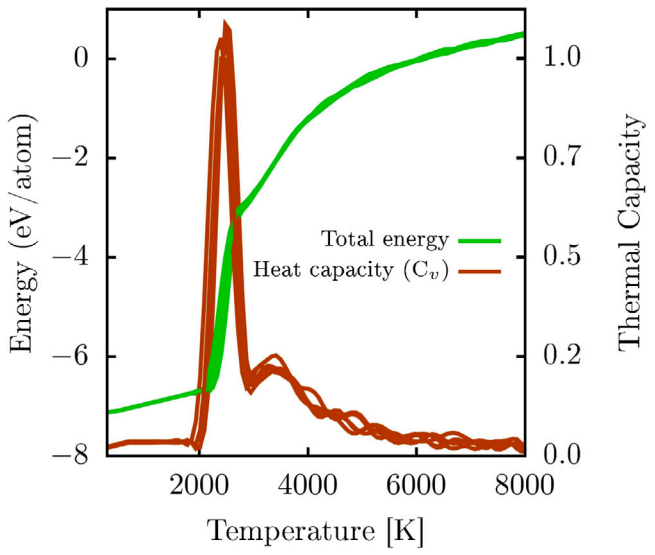

Fig. 3. Total energy (green) and heat capacity (C_V) (orange) of a PAI-G monolayer as a function of temperature for the five heating simulations. (For interpretation of the references to color in this figure legend, the reader is referred to the web version of this article.)

monolayer. These selected moments at specific temperatures detail the entire melting process of the system. Fig. 4(a) depicts the system's initial state after the equilibration and thermalization (300 K). At an order of magnitude above (2140 K, Fig. 4(b)), in terms of system temperature, PAI-G shows no phase transition with some lattice defects, remaining reasonably stable in this temperature range. At 2280 K, Fig. 4(c) displays the system partially melted but still with regions exhibiting high crystallinity of PAI-G. The melting process of the system begins at this temperature, and it is concluded at approximately 3200 K, involving the formation of nano-pores in the monolayer and the appearance of Linear Atomic Chains (LACs), as illustrated in Fig. 4(c). This trend marks the collapse point of the system, transitioning away from being a monolayer. Beyond this point, at 8000 K (Fig. 4(d)), LACs begin to disperse, and the material adopts a carbon gas form.

3.2. Mechanical characterization

We now discuss the mechanical properties of PAI-G and PAI-GNTs. Fig. 5 illustrates the stress–strain curves for PAI-G monolayers. Stress is computed as $\sigma_{x,y} = \sum_i S_{xx,yy}/V_{2D}$, where $S_{xx,yy} = -mv^2_{xx,yy} - W_{xx,yy}$ represents the stress tensor for each atom i along directions x or y. Here, the first term denotes the kinetic energy contribution of atom i, and $W_{xx,yy}$ signifies the virial contribution from interatomic interactions [38]. The effective volume of the system, denoted as V_{2D}, is determined by $V_{2D} = l_x \cdot l_y \cdot d_0$, with l_x and l_y representing the box dimensions in the x and y directions, respectively, and d_0 denoting the thickness of the system. For consistency with graphene, we set $d_0 = 3.5$ Å [45].

In Fig. 5, the stress–strain curves with uniaxial stress applied in the x and y directions are depicted in Figs. 5(a) and 5(b), respectively. In both cases, the abrupt transition between the elastic and plastic regimes is observed near the total fracture of the system. Furthermore, the consistency of the model applied here is evident in the parity of the curves concerning the different initial velocity configurations. In Fig. 5(a), with strain applied in the x direction, a linear regime is observed up to a strain close to 10% of the length of the structure in that direction. This initial linear behavior confirms the absence of material roughness and the presence of atoms out of the plane in the dimensions investigated here. In this linear region, between 0 and 1%, a fit was performed to obtain the Young's modulus (Y_M) of the material in this direction. For strain in the x direction, PAI-G exhibits $Y_M = 706.60 \pm 70.76$ GPa, which corresponds to approximately 75% of Young's modulus of graphene [46]. This case's critical stress σ_C occurs at 83.91 ± 1.49 GPa, along with the critical strain ε_C of approximately 13.64 ± 0.38%.

Table 2
Elastic constants for strains in x and y of PAI-G.

Strain direction	Y_M (GPa)	σ_C (GPa)	ε_C (%)
x	706.60 ± 70.76	83.91 ± 1.49	13.64 ± 0.38
y	815.20 ± 35.42	94.48 ± 0.96	14.10 ± 0.26

Fig. 5(b) shows the results for the strain applied in the y direction. The system behaves similarly to the case of the x direction. Still, it appears stiffer, with $Y_M = 815.20 \pm 35.42$ GPa. Its fracture occurs with a smaller strain at $\varepsilon_C = 14.10 \pm 0.26$%, with critical stress of $\sigma_C = 94.48 \pm 0.96$ GPa. This slight additional stiffness can be understood from the bonds involving both directions of PAI-G, which has a more significant number of bonds with closer alignment to the y direction than the x direction, generating higher stress for an equivalent strain in this direction. Similar to the x direction, strain in y in only one case involves the formation of LACs after the system's collapse, with total rupture around 15%. Detailed information on the elastic constants of PAI-G is presented in Table 2.

Figs. 6 and 7 illustrate representative MD snapshots for the stress–strain interplay in x and y directions presented in Fig. 5, respectively. To better elucidate the stress distribution in the system, the von Mises tensor (σ^i_{VM}) was used as it provides local information about the accumulated stress. The σ^i_{VM} for atom i is defined as:

$$\sigma^i_{\mathrm{VM}} = \sqrt{\frac{(\sigma^i_{xx} - \sigma^i_{yy})^2 + (\sigma^i_{yy} - \sigma^i_{zz})^2 + (\sigma^i_{xx} - \sigma^i_{zz})^2 + 6\left((\sigma^i_{xy})^2 + (\sigma^i_{yz})^2 + (\sigma^i_{zx})^2\right)}{2}}, \tag{1}$$

where σ^i_{xx}, σ^i_{yy}, and σ^i_{zz} are the normal stress components, and σ^i_{xy}, σ^i_{yz}, and σ^i_{zx} are the shear stress components. The VM stress helps to reveal the regions that accumulate stress and, consequently, the first bond to break.

In Fig. 6(a), the PAI-G is strained in the x direction by 1%. This material supports stress without bond breakings until 13% of strain, as illustrated in Fig. 6(b). In Fig. 6(c), one can note that at 14% of strain, the system fractures rapidly into two parts, leading to the formation of highly tensioned LACs, ultimately resulting in the total fracture of the system at 20% of strain, as depicted in Fig. 6(d). The fracture propagates perpendicularly to the direction of the applied strain. This fracture process is consistent with the trend for the stress–strain curves presented above. It is worth mentioning that the fracture process in the x direction is analogous when the tensile loading is applied in the y direction, as shown in Figs. 7(a–d).

The same stretching process was applied to study PAI-GNTs. The stress in the nanotubes is calculated similarly to the 2D systems, with $\sigma_z = \sum_i S_{zz}/V_{1D}$. Once again, the first and second terms correspond to the kinetic energy contribution and the virial contribution in the z direction. However, the effective volume of the system should not take into account the inner part of the tube, so $V_{1D} = |\vec{C}_h| \cdot |\vec{T}| \cdot d_0$ in each case.

The six different nanotubes studied here were discussed in the previous section, and their structural characteristics are presented in Table 1. In this way, Fig. 8 shows the different simulations (distinct initial velocity configurations) for all PAI-GNTs investigated here. In the case of PAI-GNT$(0, n)$ systems, the translation vector $\vec{T}_{(0,n)}$ is parallel to the lattice vector $\vec{a}$, which also corresponds to the strain direction. Thus, it is expected that for nanotubes with a larger diameter, the stress–strain characteristics and the elastic constants will approach the case of 2D strain in x due to the decrease in system curvature. The

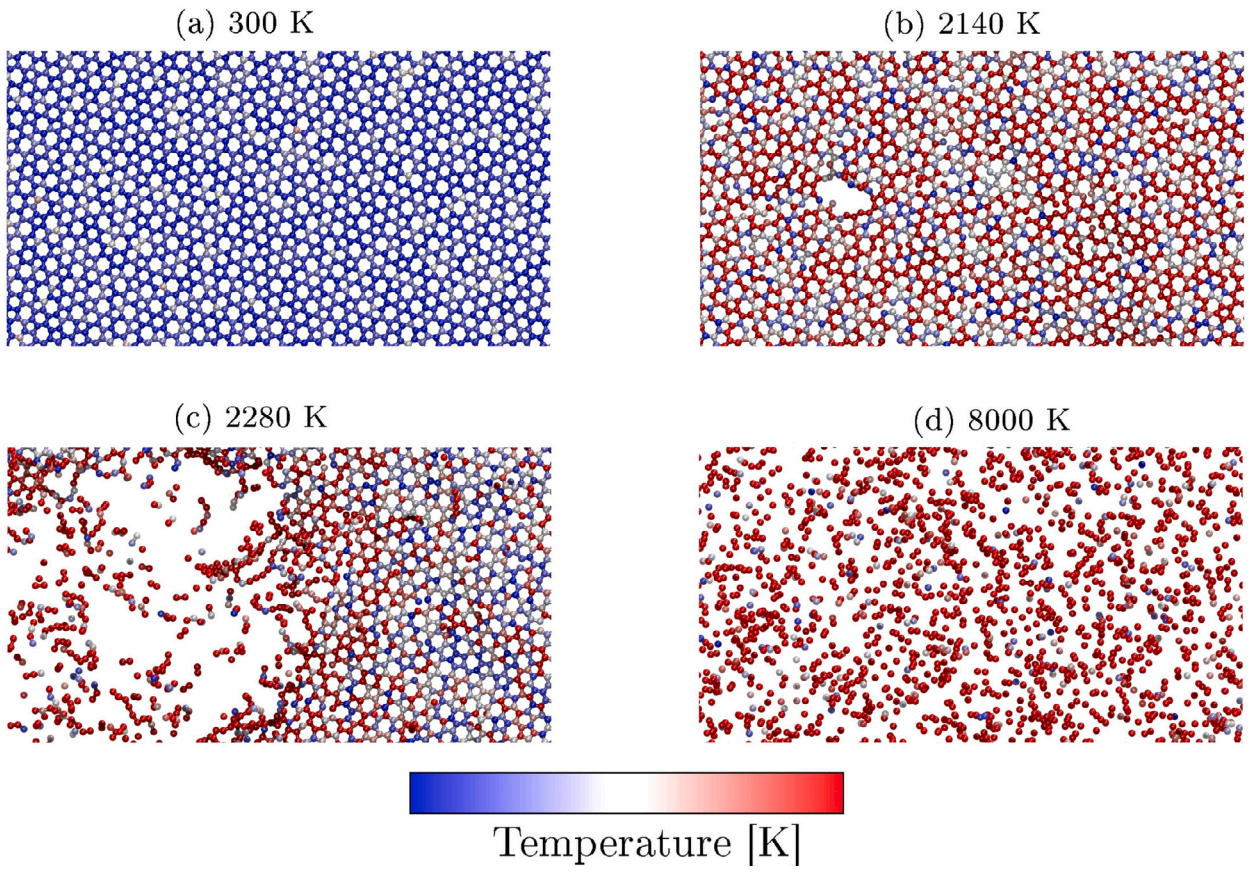

Fig. 4. Representative MD snapshots of the temperature variation in a PAI-G monolayer. Panels (a) to (d) depict the system at temperatures of 300, 2140, 2280, and 8000 K, respectively.

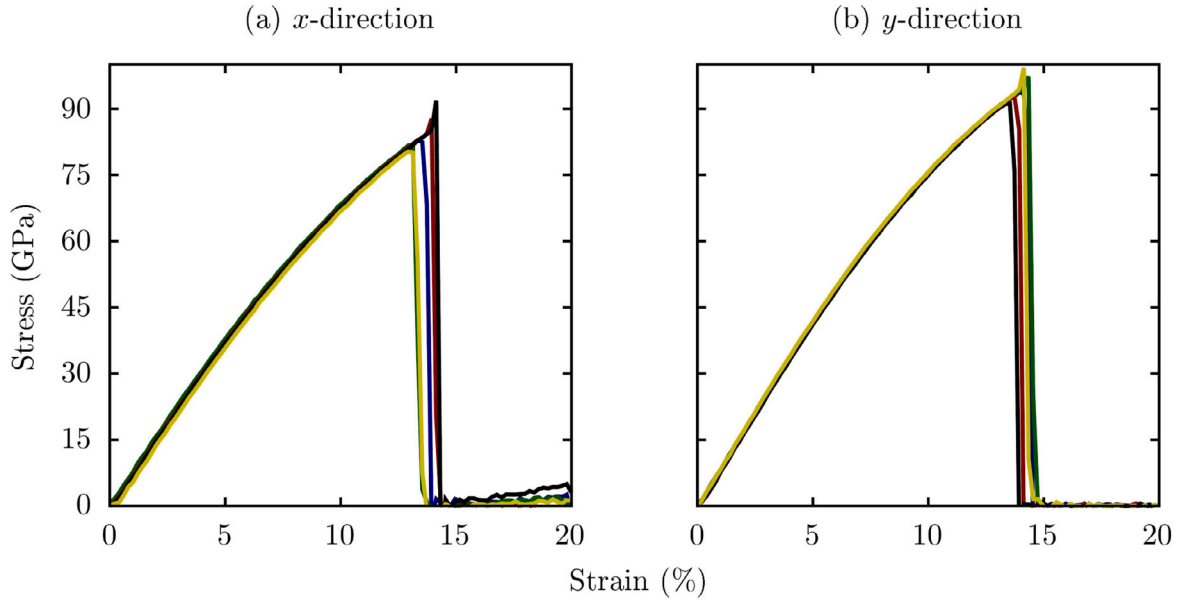

Fig. 5. Stress–strain curves of PAI-G with uniaxial strain in the (a) x direction and (b) y direction.

same trend holds for PAI-GNT(m, 0) nanotubes, whose strain direction is the vector $\vec{T}_{(m,0)} \parallel \vec{b}$, which resembles, in larger diameters, PAI-G monolayers subjected to strain in y.

In Fig. 8(a), the case PAI-GNT(0,2) system is presented. With a diameter close to 5 Å, this system exhibits significant curvature, with greater angle variation between atoms than PAI-G. Additionally, there are Van der Waals (VdW) interactions between its inner walls. These factors contribute to a system with lower stability than tubes with larger diameters or the 2D topology. It can be observed that the stress–strain curve pattern is similar to the case of 2D strain in the x direction, as discussed above. However, plateaus are presented after the critical strain, denoting the constant bond reconstructions imposed by the small

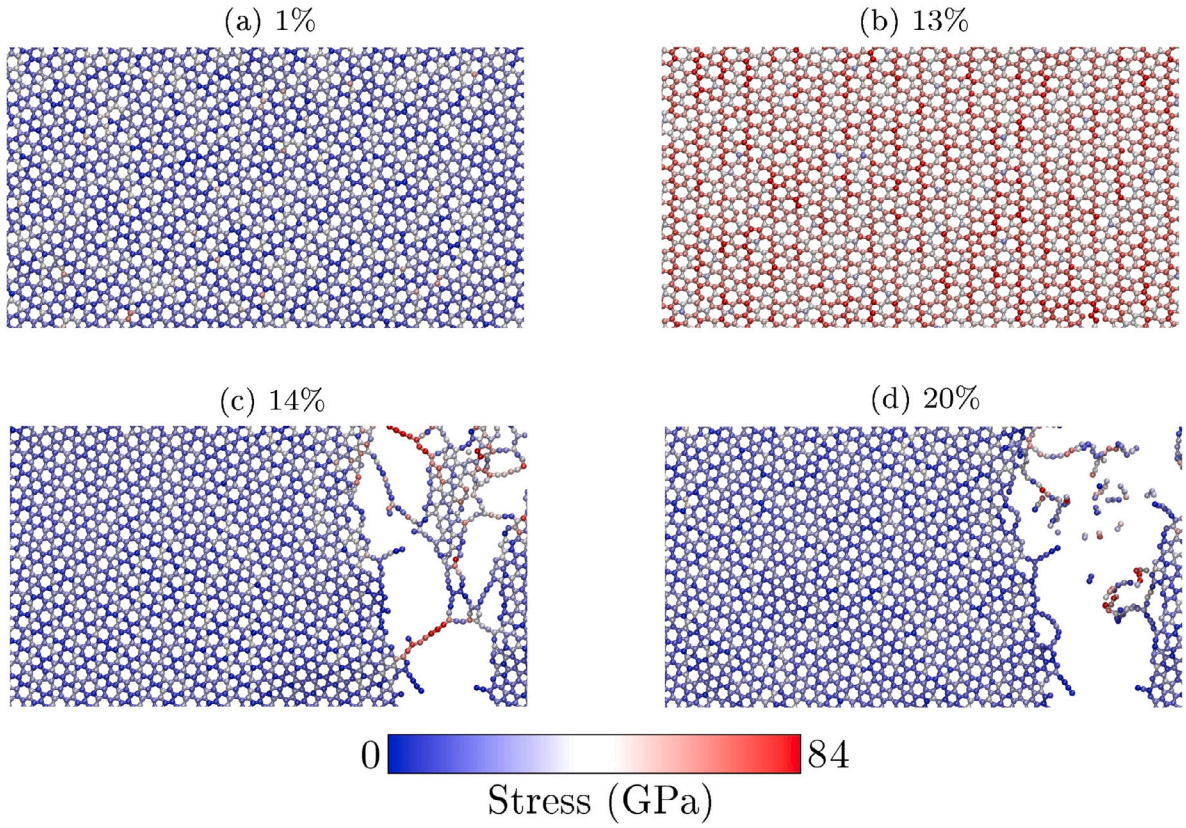

Fig. 6. Representative MD snapshots for the tensile loading simulation of PAI-G in the *x* direction. Panels (a) to (d) show 1, 13, 14, and 20% strain levels, respectively. The color coding corresponds to the von Mises stress. (For interpretation of the references to color in this figure legend, the reader is referred to the web version of this article.)

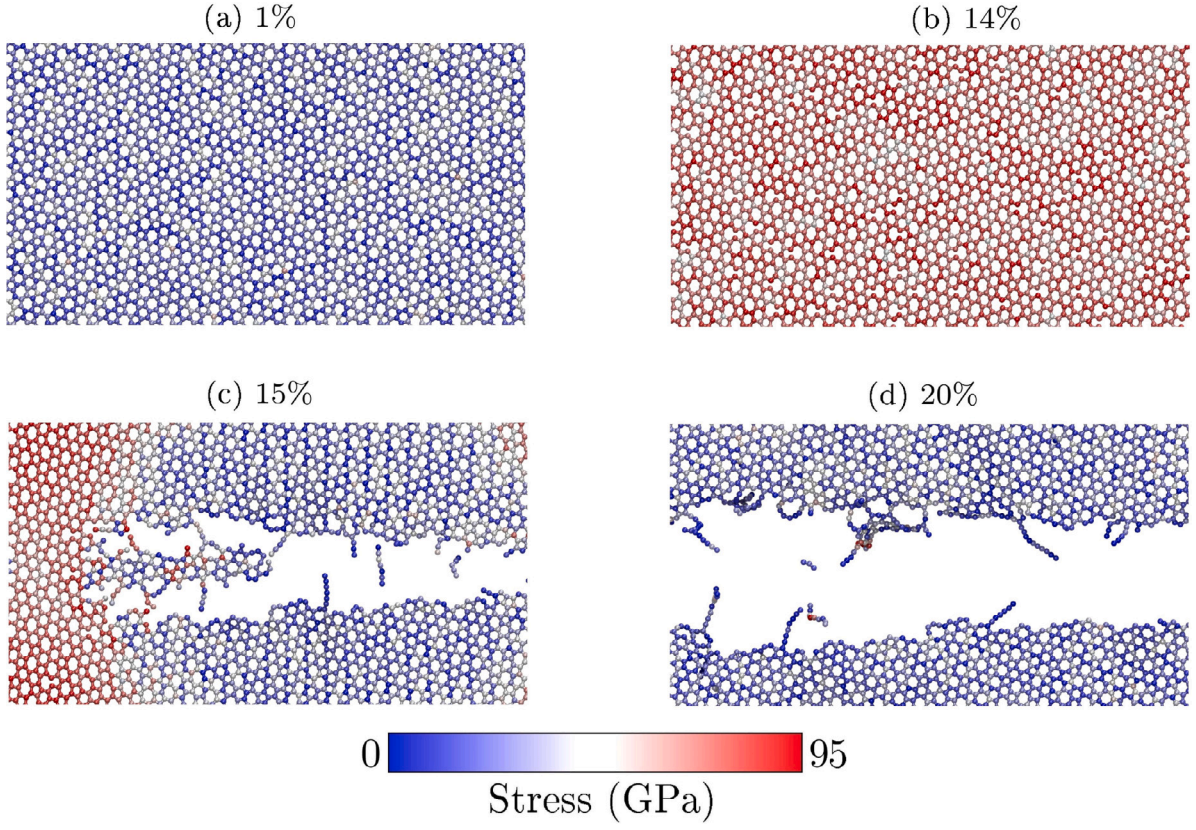

Fig. 7. Representative MD snapshots for the tensile loading simulation of PAI-G in the *x* direction. Panels (a) to (d) show 1, 14, 15, and 20% strain levels, respectively. The color coding corresponds to the von Mises stress. (For interpretation of the references to color in this figure legend, the reader is referred to the web version of this article.)

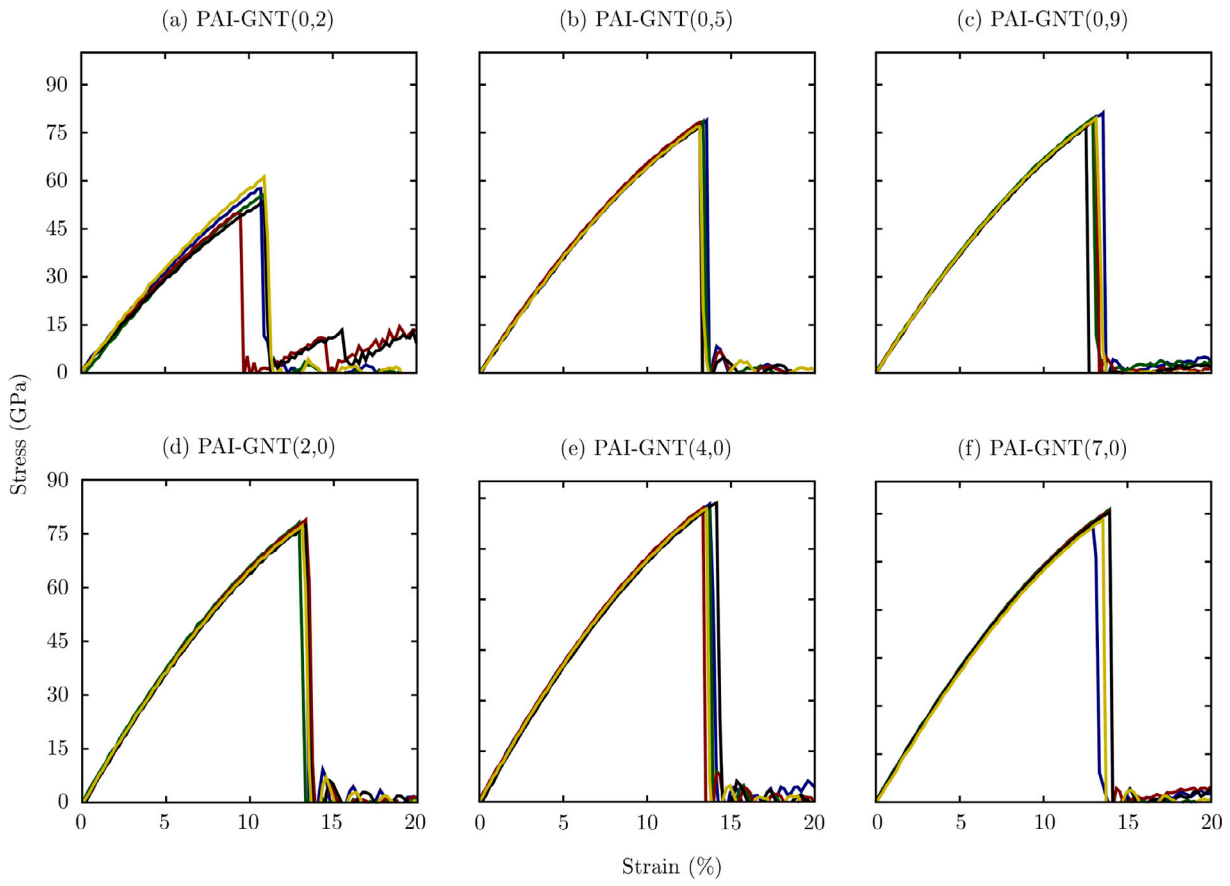

Fig. 8. Stress–strain relationship for the PAI-GNT(m,n) systems studied here with different chiralities, $(m \neq 0 \wedge n = 0)$ (a–c) $\vee(m = 0 \wedge n \neq 0)$ (d–f), and diameters. Different colors in each panel represent different initial configurations used under the same conditions. (For interpretation of the references to color in this figure legend, the reader is referred to the web version of this article.)

Table 3
Elastic constants of PAI-GNTs.

Chirality (m,n)	Y_M (GPa)	σ_C (GPa)	ε_C (%)
PAI-GNT(0,2)	657.17 ± 29.08	56.50 ± 3.64	10.68 ± 0.61
PAI-GNT(0,5)	785.09 ± 4.82	78.32 ± 0.76	13.33 ± 0.18
PAI-GNT(0,9)	807.86 ± 6.46	79.63 ± 1.45	13.10 ± 0.33
PAI-GNT(2,0)	808.74 ± 5.54	78.90 ± 0.58	13.31 ± 0.13
PAI-GNT(4,0)	872.20 ± 1.97	88.21 ± 0.85	13.77 ± 0.32
PAI-GNT(7,0)	891.62 ± 11.59	89.96 ± 1.56	13.71 ± 0.34

tube diameter. Despite still being a ductile fracture, unlike PAI-G, the transition between elastic and collapsed states is still abrupt.

Regarding the elastic constants of PAI-GNT(0,2), Y_M for this diameter is 657.17 ± 29.08 GPa. This error in calculating Y_M is attributed to the system's unstable characteristics, and it is 20% lower than the average value for the 2D system. Similarly, the average critical stress is $\langle\sigma_C\rangle = 56.60 \pm 3.64$ GPa, also about 20% less than the 2D case. The system's critical strain is slightly smaller than the one for the 2D case, supporting a strain of 10.68 ± 0.61%. This trend occurs due to the small degree of atomic reorganization in 1D systems. The PAI-GNT(0,5) and PAI-GNT(0,9) nanotubes are depicted in panels (b) and (c) of Fig. 8. The discussion for the smaller diameter case (PAI-GNT(0,2)) extends to these cases. However, as the diameter increases, the system approaches the 2D case. Note that the plastic regime decreases considerably from PAI-GNT(0,2) to PAI-GNT(0,5) and, consequently, to PAI-GNT(0,9).

In Fig. 8, panels (d) to (f), the stress response of nanotubes to longitudinal strain for chiralities $(m,0)$ is presented, indicating structurally the same strain direction as PAI-G in the y direction. Similar to the $(0,n)$ tubes, the PAI-GNT(2,0), with a smaller diameter, exhibits higher instability, with plastic strain in some initial sets. Due to its topological characteristics, its elastic constants are relatively distant from PAI-G (strained in y). Young's modulus is 808.74 ± 5.54 GPa, while the critical stress is around 78.90 ± 0.58 GPa, and the critical strain is 13.31 ± 0.13 %. This configuration has the highest standard deviation among all analyzed systems. This trend is because some initial configurations form distinct plastic strain regions. Figs. 8(e) and 8(f) show systems with the same chirality but a larger diameter. Among those studied here, PAI-GNT(4,0) has elastic characteristics quite close to those of the PAI-G sheet. The mean values of Y_M, σ_C, and ε_C are 872.20 ± 1.97 GPa, 88.21 ± 0.85 GPa, and 13.77 ± 0.32 %, respectively, with considerably low errors. None of these values deviates more than 10% from the 2D topology. In the case of PAI-GNT(7,0), the characteristics are similar to PAI-G. All elastic constants are detailed in Table 3.

To illustrate the complete strain process of the nanotubes discussed above, Figs. 9 and 10 show the representative MD snapshots for the PAI-GNT(0,5) and PAI-GNT(4,0) systems, respectively. These systems were chosen to represent the intermediate diameters studied here, covering both chiralities. In Fig. 9(a), the system with 1% strain is depicted, where the lack of tension (VM stress) along the entire nanotube can be verified. In contrast, Fig. 9(b) shows the system at its critical stress (σ_C), i.e., just after starting the plastic strain regime at 13% of strain. In Fig. 9(c), the first bond breaks at 13.2% of strain. PAI-GNT(0,5) rapidly undergoes a complete fractured form at 15.5% of strain, as illustrated in Fig. 9(d).

In Fig. 10(a), PAI-GNT(4,0) is depicted with 1% strain. This system is stiffer than the ones with the $(0,n)$ chirality. Fig. 10(b) presents the system at the critical stress, about 13.77% of strain. After this critical value, the plastic strain region takes place. The nanotube is separated into two fragments by a LAC at 17%, as depicted in Fig. 10(c). At 20%

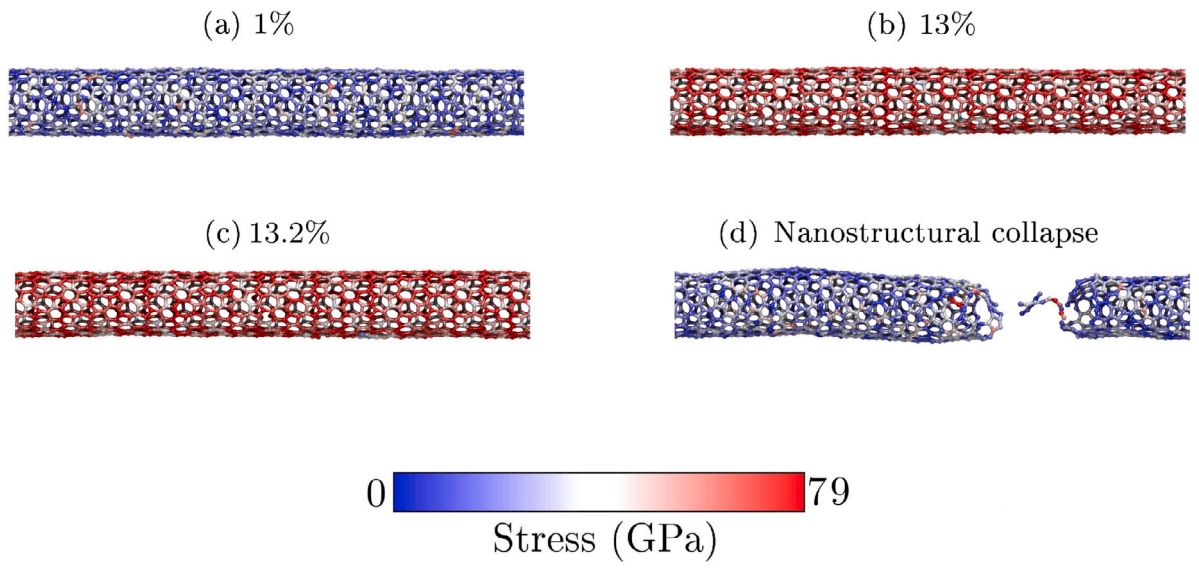

Fig. 9. Representative MD snapshots for the tensile loading simulation of PAI-GNT(0,5). Panels (a) to (d) show 1.0, 13.0, 13.2, and 15.5% strain levels, respectively. The color coding corresponds to the von Mises stress. (For interpretation of the references to color in this figure legend, the reader is referred to the web version of this article.)

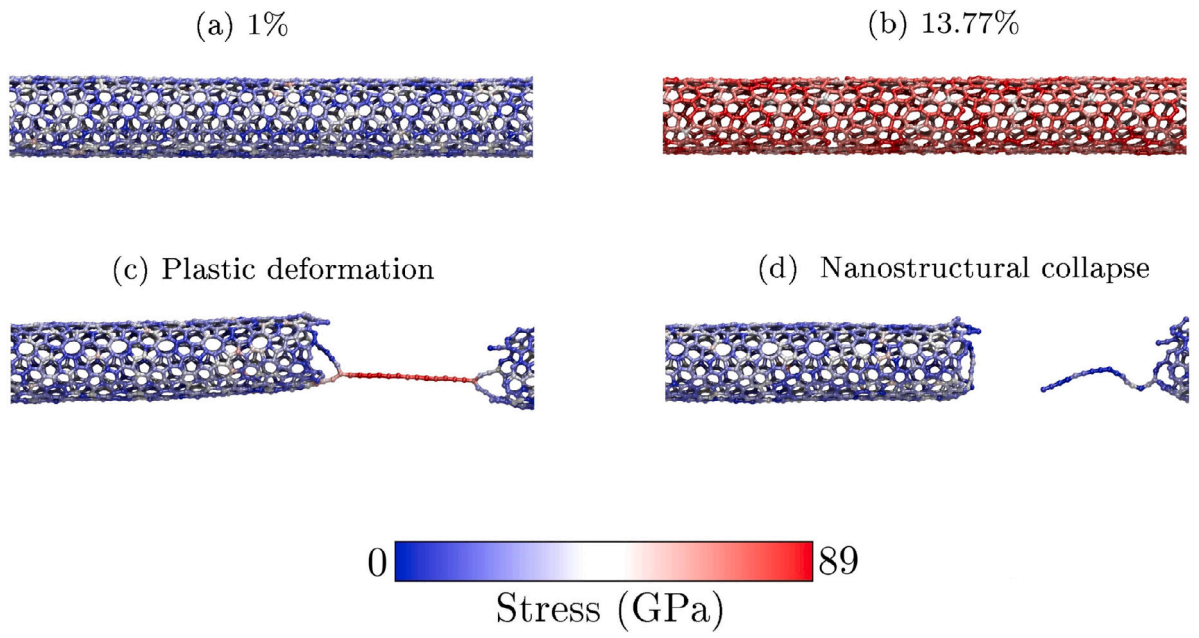

Fig. 10. Representative MD snapshots for the tensile loading simulation of PAI-GNT(4,0). Panels (a) to (d) show 1.0, 13.77, 17.0, and 20.0% strain levels, respectively. The color coding corresponds to the von Mises stress. (For interpretation of the references to color in this figure legend, the reader is referred to the web version of this article.)

of strain, the LAC is broken, and the nanotube is considered fractured, as shown in Fig. 10(d).

Finally, to further characterize the mechanical response of PAI-G, Fig. 11 presents the evolution of the relative quantity of C–C bonds with sp^1, sp^2, and sp^3 hybridizations for strains in the x (Fig. 11(a)) and y (Fig. 11(b)) directions. These characteristics were also obtained for nanotubes, but curvature did not significantly alter the hybridization of C–C bonds. It can be observed that the system is primarily composed of C–C bonds with sp^2 hybridization without the application of strain, as reported in the original PAI-G proposal article [11]. With increasing strain, a conversion of sp^2-type bonds to sp^3-type bonds occurs, stemming from increased bond length due to strain and a change in the 120° angle typical of sp^2 hybridization. In Fig. 11(a), where the system is strained in the x direction, almost 45% of the sp^2-type bonds are converted into sp^3-type bonds before the lattice fracture. In Fig. 11(b), with strain in the y direction, around 50% of sp^2-type bonds are converted to sp^3 ones. In both cases, as they result from a direct transition from elastic to complete rupture, the bonds return to their original state before strain. Around 4% of the system's hybridization remains in sp^3 due to the rearranged bonds in the fracture region. Throughout the strain process, the presence of sp^1 bonds is practically nonexistent. Still, they do exist in forming LACs in a relatively small (relative) quantity. Overlapping points are observed as different initial velocity configurations are presented.

4. Conclusion

In summary, fully atomistic simulations were conducted to investigate the thermal and mechanical characterization of monolayers and nanotubes of PAI-Graphene, a recently proposed allotrope. The study involved simulations of system heating to obtain the energetic response

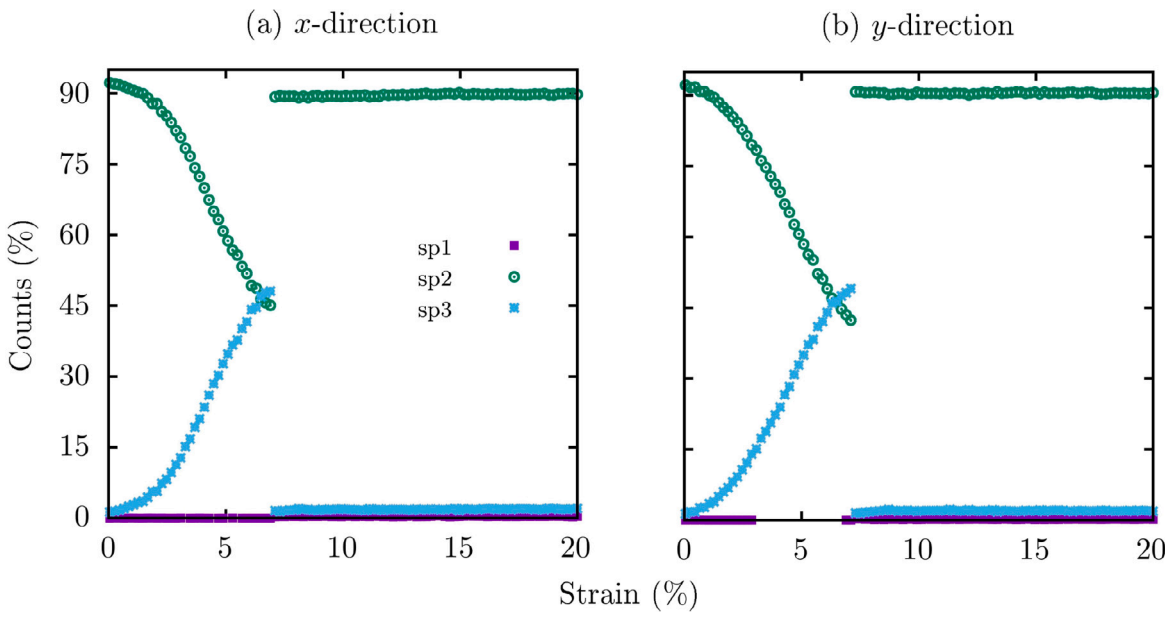

Fig. 11. Relative number of sp^1 (cross point), sp^2 (triangular point), and sp^3 (circular point) C–C bond hybridizations for PAI-G strained in the (a) x and (b) y directions.

of PAI-G and examine the mechanical response by applying uniaxial strain to the materials in flat and tubular shapes.

Results indicate that PAI-G has a higher melting point than graphene, approximately 3200 K. When strained in the x direction, the monolayer of PAI-G exhibits Young's modulus of 706 GPa. In contrast, in the y direction, it demonstrates a stiffer behavior, with Young's modulus of 815 GPa. The fracture of these systems is ductile, with critical strain values of 13% and 14% for strains in the x and y directions, respectively. The maximum stress at the moment of strain reaches 83 GPa and 94 GPa for strains in the x and y directions, respectively.

Regarding nanotubes, the smaller the diameter, the less rigid the system, with Young's modulus ranging from 650 GPa to 895 GPa. The larger the diameter, the closer the mechanical response of the system is to the monolayer. Additionally, it was found that the C–C bond hybridization of PAI-G is predominantly sp^2, with conversion to sp^3 during the strain process and before the lattice fracture.

CRediT authorship contribution statement

Rodrigo A.F. Alves: Writing – original draft, Visualization, Software, Formal analysis, Data curation. **William F. Giozza:** Writing – original draft, Investigation, Funding acquisition, Formal analysis, Data curation. **Luiz A. Ribeiro Jr:** Writing – review & editing, Validation, Supervision, Investigation, Funding acquisition, Formal analysis, Conceptualization. **Marcelo L. Pereira Jr:** Writing – review & editing, Validation, Supervision, Project administration, Methodology, Investigation, Funding acquisition, Formal analysis, Conceptualization.

Declaration of competing interest

The authors declare the following financial interests/personal relationships which may be considered as potential competing interests: William Ferreira Giozza reports financial support was provided by Foundation for Research Support of the Federal District. Luiz Antonio Ribeiro Junior reports financial support was provided by Foundation for Research Support of the Federal District. Marcelo Lopes Pereira Junior reports financial support was provided by Foundation for Research Support of the Federal District. Luiz Antonio Ribeiro Junior reports financial support was provided by Coordination of Higher Education Personnel Improvement. If there are other authors, they declare that they have no known competing financial interests or personal relationships that could have appeared to influence the work reported in this paper.

Data availability

Data will be made available on request.

Acknowledgments

This work received partial support from Brazilian agencies CAPES, CNPq, and FAPDF. W.F.G. acknowledges the financial support from FAP-DF, Brazil grant 00193-00001782/2023-42. L.A.R.J. acknowledges CAPES, Brazil for partially financing this study – Finance Code 88887.691997/2022-00. CENAPAD-SP (Centro Nacional de Alto Desenpenho em São Paulo – Universidade Estadual de Campinas – UNICAMP) provided computational support for L.A.R.J and M.L.P.J (proj634, and proj960). L.A.R.J thanks the financial support from Brazilian Research Council FAP-DF grant 00193.00001808/2022-71, FAPDF-PRONEM, Brazilgrant 00193.00001247/2021-20, 00193-00001857/2023-95, and CNPq, Brazil grants 350176/2022-1. M.L.P.J acknowledges the financial support from FAP-DF, Brazil grant 00193-00001807/2023-16. L.A.R.J and M.L.P.J also thank Núcleo de Computação de Alto Desempenho (NACAD) for computational facilities through the Lobo Carneiro Supercomputer. We extend our gratitude to Ph.D. Bohayra Mortazavi for insightful discussions and valuable support on MLIP training.

Appendix A. Supplementary data

Supplementary material related to this article can be found online at https://doi.org/10.1016/j.mtcomm.2024.109591.

References

[1] Natalie Briggs, Shruti Subramanian, Zhong Lin, Xufan Li, Xiaotian Zhang, Kehao Zhang, Kai Xiao, David Geohegan, Robert Wallace, Long-Qing Chen, et al., A roadmap for electronic grade 2D materials, 2D Mater. 6 (2) (2019) 022001.
[2] Kostya S. Novoselov, Andre K. Geim, Sergei V. Morozov, De-eng Jiang, Yanshui Zhang, Sergey V. Dubonos, Irina V. Grigorieva, Alexandr A. Firsov, Electric field effect in atomically thin carbon films, science 306 (5696) (2004) 666–669.
[3] Tibor Braun, Andras Schubert, Sandor Zsindely, Nanoscience and nanotecnology on the balance, Scientometrics 38 (1997) 321–325.
[4] Chun Hung Lui, Li Liu, Kin Fai Mak, George W. Flynn, Tony F. Heinz, Ultraflat graphene, Nature 462 (7271) (2009) 339–341.
[5] Andre Konstantin Geim, Graphene: Status and prospects, science 324 (5934) (2009) 1530–1534.

[6] Andre K. Geim, Konstantin S. Novoselov, The rise of graphene, Nat. Mater. 6 (3) (2007) 183–191.

[7] Meryl D. Stoller, Sungjin Park, Yanwu Zhu, Jinho An, Rodney S. Ruoff, Graphene-based ultracapacitors, Nano Lett. 8 (10) (2008) 3498–3502.

[8] A.H. Castro Neto, Francisco Guinea, Nuno M.R. Peres, Kostya S. Novoselov, Andre K. Geim, The electronic properties of graphene, Rev. Modern Phys. 81 (1) (2009) 109.

[9] K. Salmalian, S. Rouhi, S. Mehran, Molecular dynamics simulations of the buckling of graphyne and its family, Physica B 457 (2015) 135–139.

[10] Raphael M. Tromer, Marcelo L. Pereira Júnior, Kleuton A. L. Lima, Alexandre F. Fonseca, Luciano R. da Silva, Douglas S. Galvão, Luiz A. Ribeiro Junior, Mechanical, electronic, and optical properties of 8-16-4 graphyne: A 2D carbon allotrope with Dirac cones, J. Phys. Chem. C (2023).

[11] Xin Chen, Adrien Bouhon, Linyang Li, François M. Peeters, Biplab Sanyal, PAI-graphene: A new topological semimetallic two-dimensional carbon allotrope with highly tunable anisotropic Dirac cones, Carbon 170 (2020) 477–486.

[12] M.L. Pereira Júnior, Wiliam Ferreira da Cunha, William Ferreira Giozza, Rafael Timoteo de Sousa Junior, L.A. Ribeiro Junior, Irida-graphene: A new 2D carbon allotrope, FlatChem 37 (2023) 100469.

[13] Zhenhai Wang, Xiang-Feng Zhou, Xiaoming Zhang, Qiang Zhu, Huafeng Dong, Mingwen Zhao, Artem R. Oganov, Phagraphene: A low-energy graphene allotrope composed of 5–6–7 carbon rings with distorted dirac cones, Nano Lett. 15 (9) (2015) 6182–6186.

[14] Bohayra Mortazavi, Electronic, thermal and mechanical properties of carbon and boron nitride holey graphyne monolayers, Materials 16 (20) (2023) 6642.

[15] Bohayra Mortazavi, Structural, electronic, thermal and mechanical properties of C60-based fullerene two-dimensional networks explored by first-principles and machine learning, Carbon 213 (2023) 118293.

[16] Yongkang Tan, Xiaoma Tao, Yifang Ouyang, Qing Peng, Stable and 7.7 wt% hydrogen storage capacity of Ti decorated Irida-Graphene from first-principles calculations, Int. J. Hydrog. Energy 50 (2024) 738–748.

[17] Neda Mousavi, Jamal Davoodi, Molecular dynamics study of the penetration resistance of graphene woven fabrics membrane impacted by nanoparticles, Comput. Mater. Sci. 214 (2022) 111766.

[18] Davide G. Sangiovanni, Ricardo Faccio, Gueorgui Kostov Gueorguiev, Anelia Kakanakova-Georgieva, Discovering atomistic pathways for supply of metal atoms from methyl-based precursors to graphene surface, Phys. Chem. Chem. Phys. 25 (1) (2023) 829–837.

[19] Qitang Fan, Linghao Yan, Matthias W. Tripp, Ondřej Krejčí, Stavrina Dimosthenous, Stefan R. Kachel, Mengyi Chen, Adam S. Foster, Ulrich Koert, Peter Liljeroth, et al., Biphenylene network: A nonbenzenoid carbon allotrope, Science 372 (6544) (2021) 852–856.

[20] Lingxiang Hou, Xueping Cui, Bo Guan, Shaozhi Wang, Ruian Li, Yunqi Liu, Daoben Zhu, Jian Zheng, Synthesis of a monolayer fullerene network, Nature 606 (7914) (2022) 507–510.

[21] Yiming Hu, Chenyu Wu, Qingyan Pan, Yinghua Jin, Rui Lyu, Vikina Martinez, Shaofeng Huang, Jingyi Wu, Lacey J. Wayment, Noel A. Clark, et al., Synthesis of γ-graphyne using dynamic covalent chemistry, Nat. Synth. 1 (6) (2022) 449–454.

[22] Chee Tat Toh, Hongji Zhang, Junhao Lin, Alexander S. Mayorov, Yun-Peng Wang, Carlo M. Orofeo, Darim Badur Ferry, Henrik Andersen, N. Kakenov, Zenglong Guo, Irfan Haider Abidi, Hunter Sims, Kazu Suenaga, Sokrates T. Pantelides, Barbaros Özyilmaz, Synthesis and properties of free-standing monolayer amorphous carbon, Nature 577 (2020) 199–203.

[23] Yuanping Chen, Yuee Xie, Xiaohong Yan, Marvin L. Cohen, Shengbai Zhang, Topological carbon materials: A new perspective, Phys. Rep. 868 (2020) 1–32.

[24] Pascal Friederich, Artem Fediai, Simon Kaiser, Manuel Konrad, Nicole Jung, Wolfgang Wenzel, Toward design of novel materials for organic electronics, Adv. Mater. 31 (26) (2019) 1808256.

[25] Daniel P. Tabor, Loïc M. Roch, Semion K. Saikin, Christoph Kreisbeck, Dennis Sheberla, Joseph H. Montoya, Shyam Dwaraknath, Muratahan Aykol, Carlos Ortiz, Hermann Tribukait, et al., Accelerating the discovery of materials for clean energy in the era of smart automation, Nat. Rev. Mater. 3 (5) (2018) 5–20.

[26] Kasra Momeni, Yanzhou Ji, Yuanxi Wang, Shiddartha Paul, Sara Neshani, Dundar E. Yilmaz, Yun Kyung Shin, Difan Zhang, Jin-Wu Jiang, Harold S. Park, et al., Multiscale computational understanding and growth of 2D materials: A review, npj Comput. Mater. 6 (1) (2020) 22.

[27] Shulin Luo, Tianshu Li, Xinjiang Wang, Muhammad Faizan, Lijun Zhang, High-throughput computational materials screening and discovery of optoelectronic semiconductors, Wiley Interdiscip. Rev.: Comput. Mol. Sci. 11 (1) (2021) e1489.

[28] Monsur Islam, Andrés Díaz Lantada, Dario Mager, Jan G. Korvink, Carbon-based materials for articular tissue engineering: from innovative scaffolding materials toward engineered living carbon, Adv. Healthc. Mater. 11 (1) (2022) 2101834.

[29] Hongya Geng, Yan Peng, Liangti Qu, Haijiao Zhang, Minghong Wu, Structure design and composition engineering of carbon-based nanomaterials for lithium energy storage, Adv. Energy Mater. 10 (10) (2020) 1903030.

[30] Zishuang Cheng, Xiaoming Zhang, Hui Zhang, Jianbo Gao, Heyan Liu, Xiao Yu, Xuefang Dai, Guodong Liu, Guifeng Chen, Two-dimensional metallic carbon allotrope with multiple rings for ion batteries, Phys. Chem. Chem. Phys. 23 (34) (2021) 18770–18776.

[31] Colin W. Glass, Artem R. Oganov, Nikolaus Hansen, USPEX—Evolutionary crystal structure prediction, Comput. Phys. Commun. 175 (11–12) (2006) 713–720.

[32] Amin Farzin, Mohammad Etemadi, Saeed Mehran, Saeed Rouhi, Investigating the mechanical properties of perfect and defective ψ-graphene: A molecular dynamics simulation, Mater. Today Commun. 37 (2023) 106908.

[33] Xiaoyin Li, Qian Wang, Puru Jena, ψ-Graphene: A new metallic allotrope of planar carbon with potential applications as anode materials for lithium-ion batteries, J. Phys. Chem. Lett. 8 (14) (2017) 3234–3241.

[34] Steve Plimpton, Fast parallel algorithms for short-range molecular dynamics, J. Comput. Phys. 117 (1) (1995) 1–19.

[35] Aidan P. Thompson, H. Metin Aktulga, Richard Berger, Dan S. Bolintineanu, W. Michael Brown, Paul S. Crozier, Pieter J. in't Veld, Axel Kohlmeyer, Stan G. Moore, Trung Dac Nguyen, et al., LAMMPS-A flexible simulation tool for particle-based materials modeling at the atomic, meso, and continuum scales, Comput. Phys. Comm. 271 (2022) 108171.

[36] Thomas C. O'connor, Jan Andzelm, Mark O. Robbins, AIREBO-M: A reactive model for hydrocarbons at extreme pressures, J. Chem. Phys. 142 (2) (2015).

[37] Marcelo L. Pereira Junior, José M. De Sousa, Wjefferson H.S. Brandão, Douglas S. Galvão, Alexandre F. Fonseca, Luiz A. Ribeiro Junior, Exploring the elastic properties and fracture patterns of Me-graphene monolayers and nanotubes through reactive molecular dynamics simulations, Chem. Phys. Lett. 830 (2023) 140812.

[38] José Moreira de Sousa, Wjefferson Henrique da Silva Brandão, Weverson Lucas Aguiar Paula Silva, Luiz Antônio Ribeiro Júnior, Douglas Soares Galvão, Marcelo Lopes Pereira Júnior, Nanomechanical behavior of pentagraphyne-based single-layer and nanotubes through reactive classical molecular dynamics, C 9 (4) (2023) 110.

[39] Marcelo Lopes Pereira Júnior, Luiz Antônio Ribeiro Júnior, Thermomechanical insight into the stability of nanoporous graphene membranes, FlatChem 24 (2020) 100196.

[40] Thomas R. Mattsson, J. Matthew D. Lane, Kyle R. Cochrane, Michael P. Desjarlais, Aidan P. Thompson, Flint Pierce, Gary S. Grest, First-principles and classical molecular dynamics simulation of shocked polymers, Phys. Rev. B 81 (5) (2010) 054103.

[41] Nicos S. Martys, Raymond D. Mountain, Velocity Verlet algorithm for dissipative-particle-dynamics-based models of suspensions, Phys. Rev. E 59 (3) (1999) 3733.

[42] William G. Hoover, Canonical dynamics: Equilibrium phase-space distributions, Phys. Rev. A 31 (3) (1985) 1695.

[43] William Humphrey, Andrew Dalke, Klaus Schulten, VMD: Visual molecular dynamics, J. Mol. Graph. 14 (1) (1996) 33–38.

[44] J.H. Los, K.V. Zakharchenko, M.I. Katsnelson, Annalisa Fasolino, Melting temperature of graphene, Phys. Rev. B 91 (4) (2015) 045415.

[45] Xiao Huang, Zongyou Yin, Shixin Wu, Xiaoying Qi, Qiyuan He, Qichun Zhang, Qingyu Yan, Freddy Boey, Hua Zhang, Graphene-based materials: synthesis, characterization, properties, and applications, small 7 (14) (2011) 1876–1902.

[46] Jin-Wu Jiang, Jian-Sheng Wang, Baowen Li, Young's modulus of graphene: A molecular dynamics study, Phys. Rev. B 80 (11) (2009) 113405.